J. Fluid Mech. (1993), *vol.* 255, *pp.* 65–90

The structure of intense vorticity in isotropic turbulence

By JAVIER JIMÉNEZ[1]†, ALAN A. WRAY[2], PHILIP G. SAFFMAN[3] AND ROBERT S. ROGALLO[2]

[1] Centre for Turbulence Research, Stanford University, Stanford, CA 94305, USA

[2] NASA Ames Research Centre, Moffett Field, CA 94035, USA

[3] Applied Mathematics, California Institute of Technology, Pasadena, CA 91125, USA

(Received 17 November 1992)

The structure of the intense-vorticity regions is studied in numerically simulated homogeneous, isotropic, equilibrium turbulent flow fields at four different Reynolds numbers, in the range $Re_\lambda = 35$–170. In accordance with previous investigators this vorticity is found to be organized in coherent, cylindrical or ribbon-like, vortices ('worms'). A statistical study suggests that they are simply especially intense features of the background, $O(\omega')$, vorticity. Their radii scale with the Kolmogorov microscale and their lengths with the integral scale of the flow. An interesting observation is that the Reynolds number γ/ν, based on the circulation of the intense vortices, increases monotonically with Re_λ, raising the question of the stability of the structures in the limit of $Re_\lambda \to \infty$. Conversely, the average rate of stretching of these vortices increases only slowly with their peak vorticity, suggesting that self-stretching is not important in their evolution. One- and two-dimensional statistics of vorticity and strain are presented; they are non-Gaussian and the behaviour of their tails depends strongly on the Reynolds number. There is no evidence of convergence to a limiting distribution in this range of Re_λ, even though the energy spectra and the energy dissipation rate show good asymptotic properties in the higher-Reynolds-number cases. Evidence is presented to show that worms are natural features of the flow and that they do not depend on the particular forcing scheme.

1. Introduction

It is generally agreed that homogeneous isotropic turbulence is approximately described by the Kolmogorov (1941) cascade theory (see, for example, Landau & Lifshitz 1959, pp. 116–123). In particular the $k^{-\frac{5}{3}}$ energy spectrum, and the almost universal scaling of the dissipation range in Kolmogorov variables, stand as two of the most successful predictions in fluid mechanics. It has also been known for a long time that this description is incomplete. It was first shown by Batchelor & Townsend (1949) that the statistics of the velocity derivatives are incompatible with an uncorrelated random behaviour of the velocity field at scales comparable to the Kolmogorov dissipation limit. This intermittent behaviour becomes more pronounced as the Reynolds number increases, and flatness factors ~ 50 have been reported in the atmospheric boundary layer (Van Atta & Antonia 1980), suggesting that any theory based on uncorrelated Gaussian field might be seriously deficient in the limit $Re \to \infty$. It has to be stressed that, even in these cases, the energy spectrum remains self-similar

† Permanent address: School of Aeronautics, Pl. Cardenal Cisneros 3, 28040 Madrid, Spain.

and agrees reasonably well with Kolmogorov's predictions. Energy, and even energy transfer, are large-scale or inertial-range phenomena, and do not seem to be strongly affected by intermittency, while the higher moments are associated with rare, intense, small-scale events which do not influence the low-order statistics.

It is not clear *a priori* whether this state of affairs will persist at large Re. Moreover, since experiments at Reynolds numbers much higher than those presently available from geophysical flows cannot be expected in the near future, some sort of theoretical understanding of the intermittent small scales is clearly desirable. In this paper we present new data from numerical isotropic homogeneous turbulence at several Reynolds numbers. Even though numerical constraints restrict our experiments to $Re_\lambda \leqslant 200$, it may be expected that the exceptional level of detail that can be derived from numerical simulations might help in the theoretical study of the phenomena.

It was discovered recently that strong coherent elongated vortices ('worms') are present among the small scales of many turbulent flow (Siggia 1981; Kerr 1985; Hosokawa & Yamamoto 1990; She, Jackson & Orszag 1990; Ruetsch & Maxey 1991; Vincent & Meneguzzi 1991; Douady, Couder & Brachet 1991), and this discovery generated considerable excitement in the turbulence community. One reason for this interest is that, being strong and therefore presumably decoupled from the influence of other flow components, the behaviour of the worms should be relatively easy to understand. Should these vortices be found to form an important part of the turbulence phenomenon, their relative simplicity would give us a tool for the analysis of at least some part of the flow. Failing that, if it could be shown that they are nothing but extreme cases of a more general population of weaker vorticity structures, it might still be true that their study contains some clues to the behaviour of those background vortices, which in turn would constitute an important part of the flow. Even if none of these possibilities turns out to be true, the strong vortices are still relatively simple objects submerged in a turbulent flow, and they may be used as probes for the flow structure.

We will show below that, of these three possibilities, the second seems to be the correct one. In terms of integrated quantities, the strong structures constitute a negligible part of homogeneous isotropic turbulent flows, although they are made conspicuous in flow visualizations by their locally high intensities. Moreover their statistical properties are generally similar to those of the background vorticity, and they seem to be just intense realizations of the latter. On the other hand, since they are easy to identify and relatively few in number for any given simulation, their behaviour can be studied easily, and can be extrapolated to a description of the behaviour of the background.

The next section discusses the numerical set-up and the general characterization of the flow fields. The univariate probability distributions of the velocity gradients are presented next, with especial emphasis on the intense region. The geometric structure of those regions is also discussed in that section. Section 4 contains some experiments on truncated fields in which the intense regions have been either isolated or discarded. The dynamics of worm formation are explored in §5 by means of two-dimensional joint probability density functions of various quantities, and by direct measurement of their geometric scaling properties, as a function of Re_λ. Finally, the results are discussed and some conclusions are offered.

Line	Re_λ	N	L	L/λ	L/η	$\epsilon L/u'^3$	$\omega' T$	t/T
–·–	35.1	64	1.97	2.55	30	1.09	9.9	12.8
.....	61.1	128	1.76	3.34	52	0.82	12.9	5.3
– – –	94.1	256	1.37	4.39	84	0.70	17.0	7.6
——	168.1	512	1.65	7.77	198	0.69	30.1	5.9

TABLE 1. Numerical and flow parameters for the four basic cases analysed in this paper. t/T is the total run time in eddy turnover units. Line types are used consistently in the figures.

2. The numerical experiments

Our observations are made on direct numerical simulations of isotropic homogeneous turbulence in triply periodic boxes at four different Reynolds numbers, ranging from $Re_\lambda = 35$ to 170. It is surprising that we are able to find similarity laws spanning the whole range of Reynolds numbers, and that even the lowest-Re_λ flow seems to be essentially turbulent. This gives us some confidence that our observations may represent asymptotic trends for high-Reynolds-number turbulence.

The numerical method is fully spectral, using primitive variables $\boldsymbol{u}, p$, with dealiasing achieved by spherical wave-space truncation and phase shifting (Canuto *et al.* 1987). The resolution N, given in table 1, reflects the number of real Fourier modes in each direction before dealiasing. The time-stepping procedure is a second-order Runge–Kutta one for the nonlinear terms and an analytic integrating factor for the viscous ones. The time step is automatically controlled to satisfy the numerical stability condition. The Fourier expansion functions are $\exp(\pm ik_j x_j), k_j = 0, 1, \ldots, K = \frac{1}{2}N$, so that the length of the box side is always 2π. Unless stated otherwise, all experiments are forced to achieve a statistically steady state. Forcing is achieved by introducing a negative viscosity coefficient for all the modes with wavenumbers $k = |\boldsymbol{k}| \leqslant 2.5$. The magnitude of the negative viscosity is adjusted every few time steps so as to keep the product $K\eta$ constant, where $\eta = (\nu^3/\epsilon)^{\frac{1}{4}}$ is the Kolmogorov scale. This forcing is arbitrary, as are most other ways of forcing turbulence, but it has the advantage of fixing automatically the numerical resolution of the scheme, and is therefore very convenient when a given simulation cannot be repeated many times, as is the case with our larger grids. Some test comparisons with other forcing methods showed no apparent differences in the results.

The instantaneous energy dissipation rate, ϵ, is computed in terms of the three-dimensional energy spectrum $E(k)$, as

$$\epsilon = \nu\omega'^2 = 2\nu \int_0^\infty k^2 E(k)\,\mathrm{d}k.$$

Other scales used in this paper are the r.m.s. velocity, defined by

$$u'^2 = \frac{2}{3}\int_0^\infty E(k)\,\mathrm{d}k,$$

the integral scale,

$$L = \frac{\pi}{2u'^2}\int_0^\infty k^{-1}E(k)\,\mathrm{d}k,$$

and the Taylor microscale, defined by $\lambda^2 = 15\nu u'^2/\epsilon$. The microscale Reynolds number is defined as $Re_\lambda = u'\lambda/\nu$, and the large-eddy turnover times as $T = L/u'$ (Batchelor 1953).

Table 1 summarizes the characteristics of the different runs. Each run was continued sufficiently long for the instantaneous spectra and other integral characteristics to become statistically steady. This typically took a few large-eddy times, which may not be long enough to guarantee absolute statistical steadiness for the large scales, but which should be enough for the small scales to reach equilibrium.

The calculations are fairly time consuming. Each eddy turnover time in the 256^3 computation took approximately 24 hours of computing time in a 128-node Intel hypercube (~ 1.5 Gflops). The 512^3 calculation was carried out in the 512-node Caltech Delta machine and took approximately three times longer per turnover time (~ 4 Gflops). In most cases, the long runs needed to achieve equilibrium were carried out at lower resolution, which was increased to its final value to accumulate the statistics. The time that it took for the small scales to attain equilibrium at the new resolution was quite short, and no significant change in the large-scale properties of the flow were observed during that process. The $Re_\lambda = 94$ field was run for $2T$ at full resolution. The $Re_\lambda = 168$ was run only for $0.3T$.

The quantities in table 1, and the spectra in the following pages, are averages over whole flow fields and over periods of time that vary between 0.25 and 6 large-eddy turnover times. The shorter averaging times correspond to the highest Reynolds numbers. In particular the 512^3 simulation at $Re_\lambda = 170$ could only be studied for a few flow fields, closely spaced in time, but its statistics were checked, whenever possible, against longer simulations at 256^3 resolution. The histograms presented later in the paper are spatial statistics averaged over several (5 to 10), reasonably spaced, moments in time. The 512^3 simulation is again the exception, with only two field separated by less than 0.1 turnover time. The temporal variation of the spectra, when normalized to their instantaneous Kolmogorov scalings, was less than 1%, but larger variations were observed in the absolute values of the dissipation ($\sim 10\%$) and of the total energy ($\sim 5\%$), with a mean oscillation period of roughly 2 turnover times.

Large deviations among instantaneous realizations were also observed in the extreme tails of the histograms, with probabilities below 10^{-3} changing by factors of up to 2. These deviations were specially noticeable in the low-Reynolds-number cases, and lasted for substantial fractions of an eddy turnover time. In some cases they could be traced to the appearance and survival of a particularly strong structure. Even in the high-Re_λ simulations, in which the larger number of small structures results in smoother statistics, this effect was present to some extent, and should be borne in mind when interpreting our observations.

Note that the dimensionless energy dissipation $\epsilon L/u'^3$ decays slowly with increasing Re_λ, but stabilizes around 0.70 in the last two cases. This is consistent with the behaviour observed by Sreenivasan (1984) in a compilation of data from grid turbulence, in which the dissipation stabilizes above approximately $Re_\lambda > 60$. His asymptotic value of the dissipation, $\epsilon L/u'^3 \approx 1$, is different from ours, but this is not surprising since the integral scale is dominated by the large eddies, which are presumably different in the two cases.

The statistics of the small-scale intense regions are sensitive to the numerical resolution. After some experimentation, it was found that $K\eta = 1$ was the absolute minimum needed for convergence of the velocity gradient histograms, and that $K\eta \approx 2$ was very desirable. We have maintained this latter resolution uniformly.

Three-dimensional, shell-averaged, energy spectra for the three cases are presented in figure 1. The two cases with the highest Re_λ show a short 'inertial' range with a power decay close to $k^{-\frac{5}{3}}$. No such interval is present at the lowest Re_λ, but the collapse of the dissipation range is satisfactory, although there appears to be a weak trend

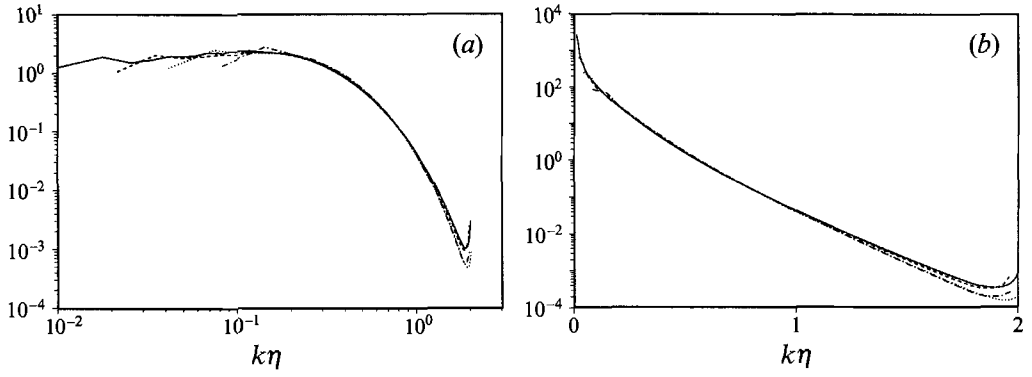

FIGURE 1. Three-dimensional energy spectra for the four different Re_λ used in this paper. (*a*) $\epsilon^{-\frac{2}{3}}k^{\frac{5}{3}}E(k)$, to display the inertial range; (*b*) $\epsilon^{-\frac{2}{3}}\eta^{-\frac{5}{3}}E(k)$, to display the dissipation range. For symbols see table 1.

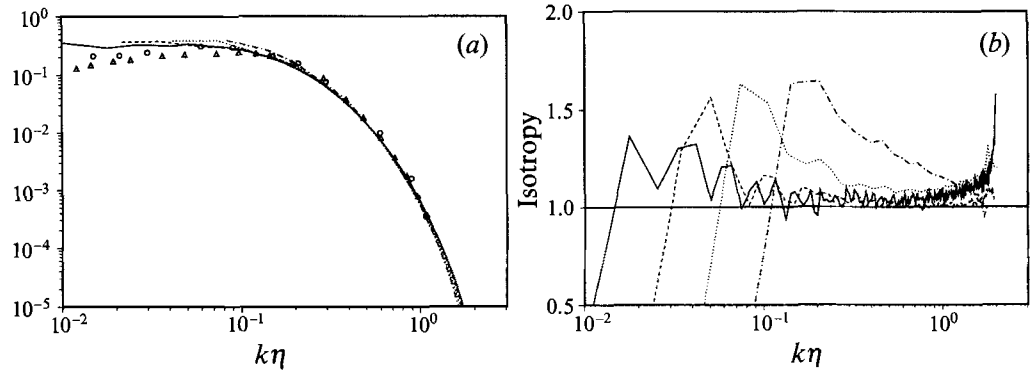

FIGURE 2. One-dimensional energy spectra for different Reynolds numbers. (*a*) Longitudinal spectra, $2\epsilon^{-\frac{2}{3}}k^{\frac{5}{3}}E_{11}(k_1)$. Lines are simulations, as in table 1. Symbols are experimental data: △, grid turbulence, $Re_\lambda = 113$ (Compte-Bellot & Corrsin 1971); ○ wake, $Re_\lambda = 182$ (Champagne 1978). (*b*) Isotropy coefficient, defined in (1).

towards fuller dissipation spectra with increasing Reynolds number. The Kolmogorov constant in the inertial range is $C_k \approx 2$. The small upturns at the highest-wavenumber end of the spectra are numerical, and reflect the incorrect representation of the turbulent cascade mechanism at wavenumbers comparable with the numerical resolution. Their comparatively small magnitudes are a measure of the numerical quality of our simulations.

Figure 2(*a*) displays one-dimensional longitudinal spectra, $E_{11}(k_1)$, which are compared to experimental results at similar Reynolds numbers. The agreement is satisfactory in the dissipation range, but there are differences in the large scales, reflecting the different types of flow. Figure 2(*b*) displays an isotropy coefficient, defined as

$$\frac{E_{11}(k_1) - k_1 \partial E_{11}(k_1)/\partial k_1}{2E_{22}(k_1)}, \tag{1}$$

where E_{22} is the transverse one-dimensional spectrum. This quantity should become equal to 1.0 for an isotropic field (Batchelor 1953), and it does so approximately for the small scales in the two high-Re_λ cases, suggesting that they have attained

equilibrium. The two cases with lower Reynolds numbers do not satisfy isotropy, clearly because of insufficient separation between the smallest and largest scales. The reason for the upturn of all the isotropy spectra at the high-wavenumber limit is not clear, but it is repetitive and survives long-time averaging. It is probably related to cross-contamination from the large energetic scales, since (1) should only be expected to be strictly satisfied when *all* the flow scales are isotropic.

In summary, the flows used in this paper seem to be typical of experimental approximations to homogeneous isotropic turbulence. It is particularly important to note that the two highest Reynolds numbers display a short $k^{-\frac{5}{3}}$ inertial range and appear to have reached the asymptotic regime in which the energy dissipation and the Kolmogorov constant become independent of the Reynolds number.

3. Worms

Implicit in the Kolmogorov (1941) model for the turbulent cascade is the idea that the small scales of turbulence are fully controlled by the viscosity ν and by the energy dissipation rate $\epsilon = \nu\omega'^2$. This, and the dimensional arguments of the original theory, imply that the velocity gradients should reach some asymptotic statistical distribution as $Re \to \infty$, whose single scale should be ω'. Evidence that this is not so has accumulated over the years, starting with the measurements of higher statistical moments mentioned earlier, and more recently in the form of increasingly non-Gaussian histograms obtained from numerical experiments at increasing Reynolds number (Siggia 1981; She *et al.* 1990; Vincent & Meneguzzi 1991; Ruetsch & Maxey 1991).

Probability density functions for longitudinal and transverse velocity gradients in our simulations are given in figure 3. It is clear that the distributions are non-Gaussian and that there is no evidence of convergence towards a limiting distribution in our Reynolds-number range. The figure also contains numerical and experimental data from previous investigators. The results of She (1991) fall well into the apparent Reynolds-number evolution of our observations. Those of Vincent & Meneguzzi (1991) seem to correspond to a slightly lower Re_λ, and are closer to what we obtain for $Re_\lambda = 170$ and lower resolution, $K\eta \approx 1$. Since their resolution was lower than ours, the discrepancy is probably numerical. Note also that the value of $Re_\lambda = 150$, given in their paper, corresponds to a definition different from ours. The only experimental data are those from Castaing, Gagne & Hopfinger (1990), in a turbulent jet at $Re_\lambda = 852$, and correspond to longitudinal velocity differences $u(x+h)-u(x)$, with $h = 3.3\eta$. They should be approximately comparable to numerical derivatives with $K\eta \approx 1$. Since our experience indicates that increasing the resolution leads to flatter histograms, theirs are probably slightly below what they should be, and the fact that they are so much flatter than ours is a strong indication that the trend in our data continues at much higher Reynolds numbers.

The high-order moments of the different distributions are given in table 2. We define the nth-order flatness or skewness of a variable ζ as $F_n = \langle\zeta^n\rangle/\langle\zeta^2\rangle^{n/2}$. In agreement with previous results, the distribution of the velocity fluctuation is independent of Reynolds number, and is slightly steeper than Gaussian, while those of the velocity gradients become increasingly non-Gaussian with Reynolds number. Note that we not only observe an increase in the flatness of the longitudinal gradients, but also a weaker but consistent increase in its skewness, which is even more apparent in F_5. An increase in skewness has been reported in observations of atmospheric flow (Van Atta & Antonia 1980) but had not been observed up to now in numerical simulations.

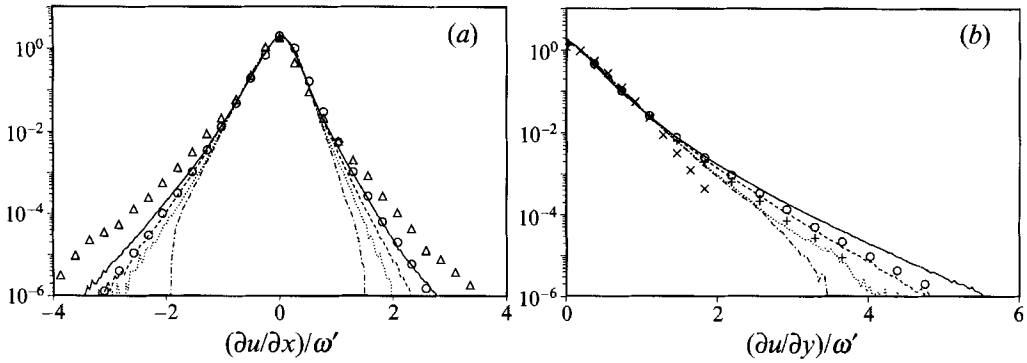

FIGURE 3. One-dimensional probability density functions for (*a*) the longitudinal and (*b*) the transverse velocity gradients. Lines are the present simulations, and follow the notation in table 1. △, Experimental data from Castaing *et al.* (1990), $Re_\lambda = 852$; ○, simulation data from Vincent & Meneguzzi (1991), $Re_\lambda = 190$; +, ×, simulations (She 1991), $Re_\lambda = 77$ and 24, respectively.

	u		$\partial u/\partial x$				$\partial u/\partial y$	
Re_λ	F_4	F_6	$-F_3$	F_4	$-F_5$	F_6	F_4	F_6
Gauss			0	3.0	0	15		
35.1	2.80	12.0	0.490	4.2	6.5	40	5.7	90
61.1	2.85	13.0	0.495	4.6	8.0	55	6.1	110
94.1	2.80	12.0	0.520	5.3	10.0	80	7.6	200
168.1	2.80	12.5	0.525	6.1	12.0	125	9.4	370

TABLE 2. Higher-order moments for the distributions of a velocity component, u, and its longitudinal and transverse gradients, $\partial u/\partial x$ and $\partial u/\partial y$. The nth-order flatness or skewness are denoted by F_n. Significant figures estimated from variation among fields. The first row contains the moments for a Gaussian distribution.

We will concentrate here on the statistics of the quantities appearing directly in the vorticity equation,

$$\frac{\frac{1}{2}\mathrm{d}|\omega|^2}{\mathrm{d}t} = \omega_i S_{ij} \omega_j + \nu \omega_i \nabla^2 \omega_i, \tag{2}$$

where $|\omega| = (\omega_i \omega_i)^{\frac{1}{2}}$ is the vorticity magnitude, and $S_{ij} = \frac{1}{2}(\partial u_i/\partial x_j + \partial u_j/\partial x_i)$ is the rate-of-strain tensor. In particular, we will be interested in the statistics of $|\omega|$, $|s| = (S_{ij} S_{ij})^{\frac{1}{2}}$, and the stretching rate

$$\sigma = \frac{\omega_i S_{ij} \omega_j}{|\omega|^2}.$$

The square of the total rate of strain, $|s|$, is proportional to the local dissipation, but it does not appear explicitly in (2). It is probably more a consequence of the events that lead to turbulence than their cause. The quantity σ is the part of the strain that is aligned with the local vorticity, and it is the term stretching the vortex lines in (2).

One-dimensional histograms for the volume fraction occupied by values of these three variables above a given threshold are given in figure 4. They are all far from Gaussian, except perhaps for the lowest Reynolds number, and show few signs of converging to a limit distribution for large Re_λ. Note however that the variable tails involve only small fractions of the total volume. The figure also contains a histogram for the fraction of the total enstrophy contributed by points with a vorticity magnitude above a given threshold. Even though the decay of this histogram is slower than that

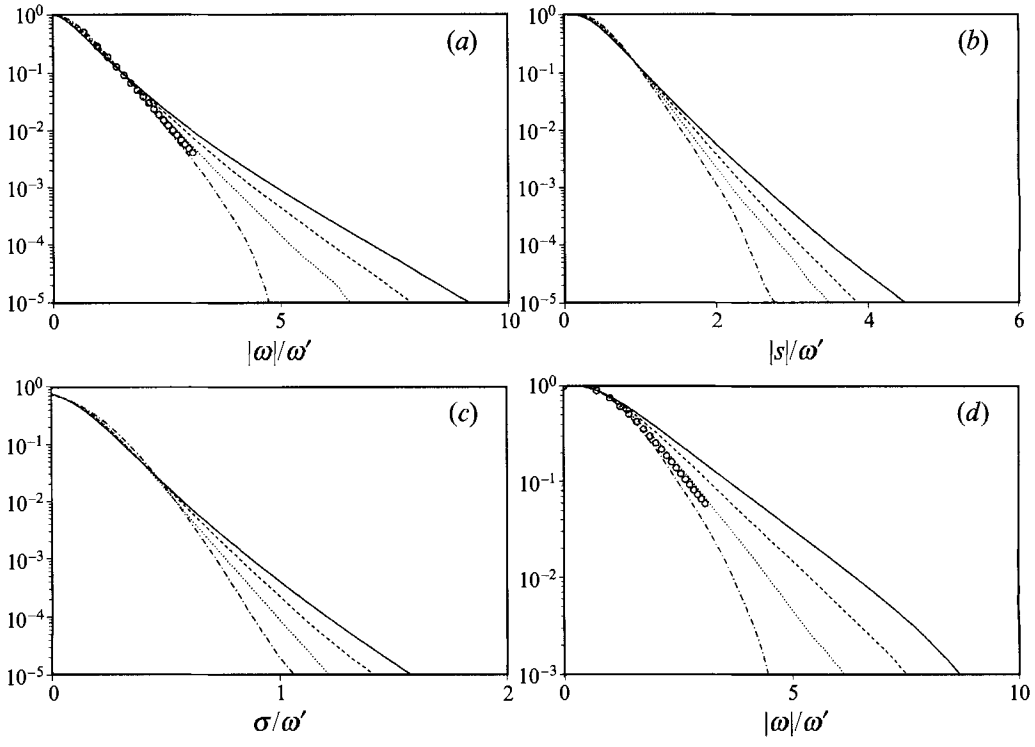

FIGURE 4. One-dimensional histograms of the volume fraction occupied by points above a certain threshold. (*a*) Vorticity, (*b*) strain rate, (*c*) stretching rate, (*d*) fraction of total enstrophy associated with points above a given vorticity magnitude. Lines as in table 1. Open circles are from Ruetsch & Maxey (1991) at $Re_\lambda = 62$.

of the volume fraction, most of the enstrophy is still contained in a relatively 'weak' background where $|\omega| \approx O(\omega')$. In fact, for the Reynolds numbers of our simulations, the contribution of the intense tails to the integrated value of any of the low-order statistics of the flow is only a few percent, although they would clearly dominate sufficiently high-order moments. Similar results were obtained by Ruetsch & Maxey (1991) at $Re_\lambda \approx 60$ (see figure 4).

The conclusion from these histograms is that most of the volume in the flow is occupied by relatively 'weak' vorticity, with strong vortices filling only a small fraction of the space. The structures of the weak and strong vorticities are also very different. Figure 5 shows a collection of vortex lines passing through randomly chosen points on the middle plane of a region within a high-Re_λ simulation, and continued until they leave the region. The vortex lines are exactly the same in both cases, but on figure 5(*a*) they are displayed only where $0.2\omega' \leqslant |\omega| \leqslant \omega'$, while on figure 5(*b*) they are displayed where $|\omega| \geqslant \omega'$. While there is little apparent structure in the low-intensity component of the flow, the strong vorticity tends to be organized in tubes or ribbons, which are the 'worms' reported in previous experiments. It is remarkable that this seems to be true even at a threshold, ω', which is much lower than the one used in most previous reports, and which still contains most of the total enstrophy.

For the rest of the paper, we will arbitrarily define *weak* vorticity as that having $|\omega| < \omega'$, *intense* vorticity, or *worms*, as that above a threshold covering 1 % of the total volume, and *background* vorticity as that above ω' but weaker than the intense threshold. This definition of worms results in pictures roughly comparable to those of

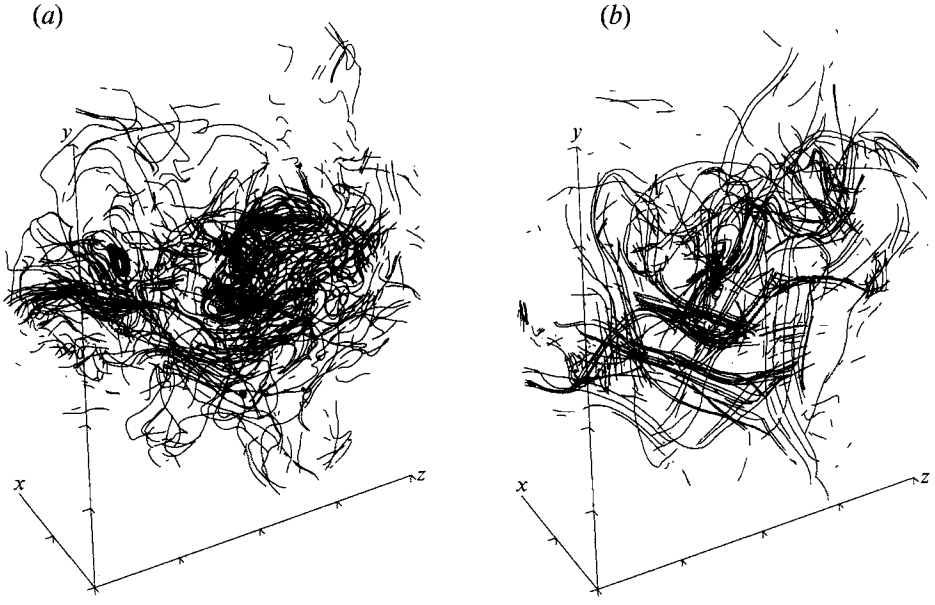

FIGURE 5. Vortex lines for homogeneous isotropic turbulence, $Re_\lambda = 168$. Length of z-axis $\approx 100\eta$. (*a*) Only $0.2\omega' < |\omega| < \omega'$; (*b*) only $|\omega| > \omega'$; vortex lines are the same in both sets.

previous workers, and is about as low as the threshold can be taken before the visual complication becomes overwhelming. Figure 5 shows that the organization into coherent structures is still present at the background level. At the Reynolds number of the figure, the vorticity above ω' fills 25% of the volume, and accounts for 80% of the total enstrophy, while intense vorticity above $3.1\omega'$ fills 1% of the volume and accounts for 15% of the enstrophy. For comparison, in a field with a Gaussian distribution for each vorticity component, vorticity magnitudes above ω' would fill 39% of the volume, and contain 70% of the enstrophy, while the 1% volume threshold would be at $1.95\omega'$, and contain 8.5% of the enstrophy.

The length of the horizontal (z) axis in figure 5 is one eighth of that of the whole cube, and one half of the integral scale of the flow. Some ribbons are seen to span the whole region, although not with uniform intensity, and they may appear disconnected in plots of the high-enstrophy worms. Intense worms, with lengths comparable to the integral scale, are found occasionally.

The shapes of the regions of highest vorticity (1%) are displayed in figure 6, at two different Reynolds numbers. In agreement with previous reports they appear to be either cylindrical vortices or ribbons of various widths. Although no real statistical analysis was made, the impression from different fields is that sheets and ribbons are predominant at low Reynolds numbers, while cylindrical vortices dominate at high Re_λ. This is apparent in figure 6, and is consistent with the idea that the worms are the results of stretching by strains which are generally not axisymmetric.

If a generic strain is applied to a weak-vorticity blob, the vorticity component along the most extensional eigenvector is amplified most, but the other two principal strains remain active and stretch or compress the vortex unequally along the two equatorial axes. As the axial vorticity becomes stronger, it dominates the local flow and its rotation tends to make the vortex axisymmetric. The result is a vortex of elliptical cross-section, whose eccentricity becomes smaller as the ratio of the axial vorticity to the driving strain becomes larger. It will be shown later that the strain is generally

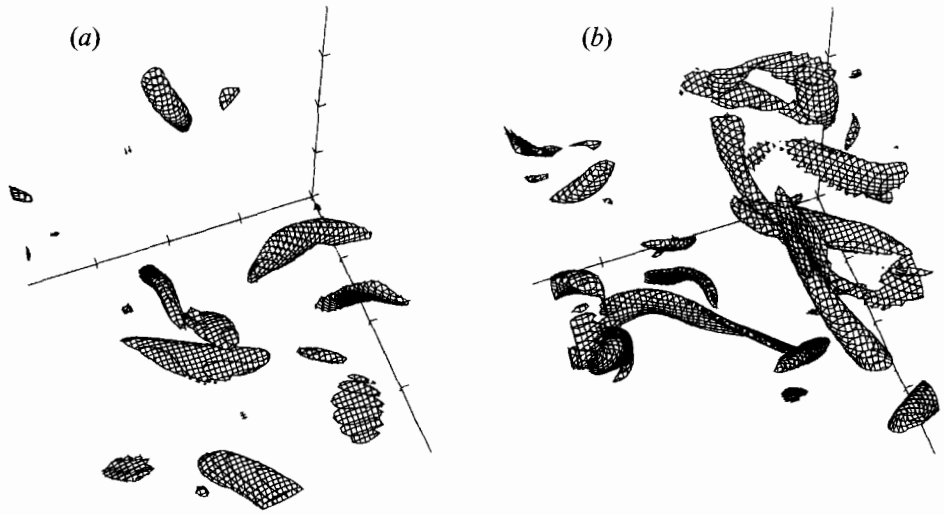

FIGURE 6. Intense-vorticity isosurfaces, $|\omega|/\omega' \geqslant 2.5$, at two different Reynolds numbers. Resolution is similar in both subsets, with the length of each axis $\approx 100\eta$. (*a*) $Re_\lambda = 63$, integral scale $L = 56\eta$; (*b*) $Re_\lambda = 95$, $L = 80\eta$. Thresholds are chosen so that worms contain about 1 % of total flow volume.

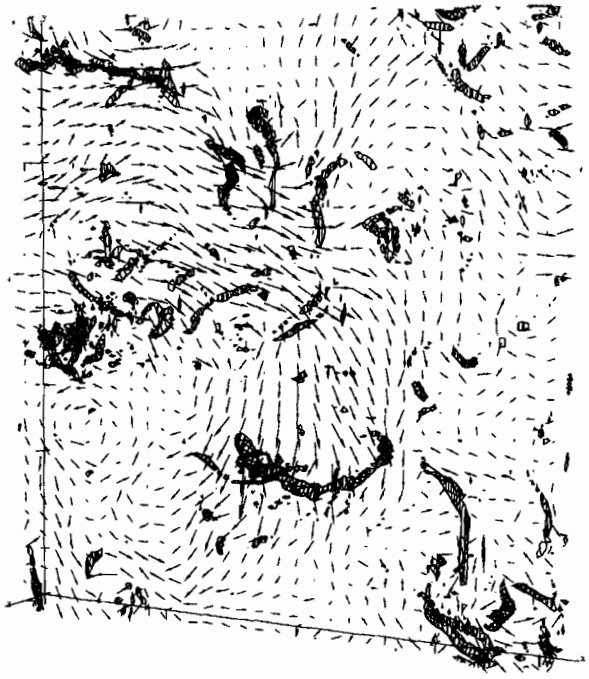

FIGURE 7. Intense-vorticity regions $|\omega| > 2.7\omega'$, and velocity field, $Re_\lambda = 168$. Size of the display domain is $(800^2 \times 50)\eta$, periodic in the two long directions. Velocity vectors correspond to points in the mid-plane.

$O(\omega')$, while it is clear from figure 4 that vortices in higher-Reynolds-number flows attain larger vorticities. This, together with the previous argument, explains their more circular cross-sections.

The spatial distribution of the worms is not uniform over scales of the order of the integral length L, although this is difficult to see in graphical representations of large

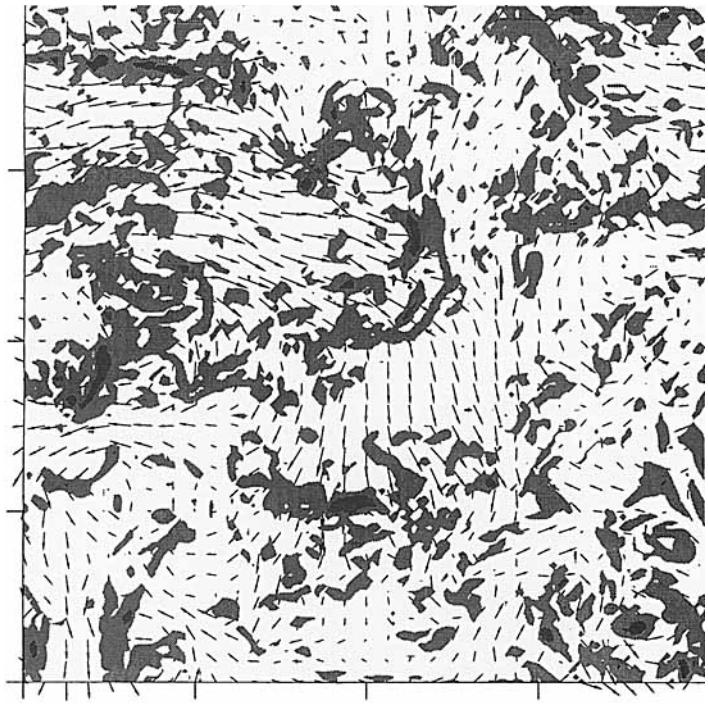

FIGURE 8. Background vorticity $|\omega| > \omega'$ (light grey), at centreplane in figure 7, in relation to darker intense regions, $|\omega| > 2.7\omega'$. Vectors are velocity.

flow volumes. Figure 7 displays a thin slab across a complete flow field. The worms are seen to lie on the borders of large-scale velocity eddies, the energy-containing scales, which are themselves relatively free from vorticity. This is even clearer in figure 8, which represents the mid-plane of the slab shown in figure 7. The light-coloured regions in this figure mark the background vorticity, $|\omega| > \omega'$. The darker regions are the worms, which are seen to be embedded in the background, of which they constitute the local maxima. The large eddies themselves are mostly free even from background vorticity, although it follows from the vorticity histograms that the magnitude of the most probable vorticity scales with ω', and that velocity gradients of the order of the driving large-scale flow, $O(u'/L)$, are relatively rare (see figure 15).

4. Truncated fields

Even though the results in the previous section suggest that, at least at these Reynolds numbers, the worms contribute relatively little to the turbulent statistics, it is conceivable that they may be important indirectly in some other respect. There is also the possibility that the worms themselves may be spurious artifacts of the forcing method, and that they would not be present in 'natural', decaying, turbulence.

To clarify these points we have carried out a series of experiments in which the worms are artificially removed from a flow, so that the properties of both the truncated field and of the isolated worms can be studied independently. Consider a flow field given by a velocity $\boldsymbol{u}(\boldsymbol{x})$ and a vorticity $\boldsymbol{\omega} = \boldsymbol{\nabla} \times \boldsymbol{u}$. We wish to generate a new field $\boldsymbol{u}_>$, associated just with the worms, by eliminating the vorticity at points where its magnitude is smaller than a given threshold, $|\omega| \leqslant \Omega$. This field cannot be constructed by simply zeroing the vorticity of the original flow at the desired points. The resulting

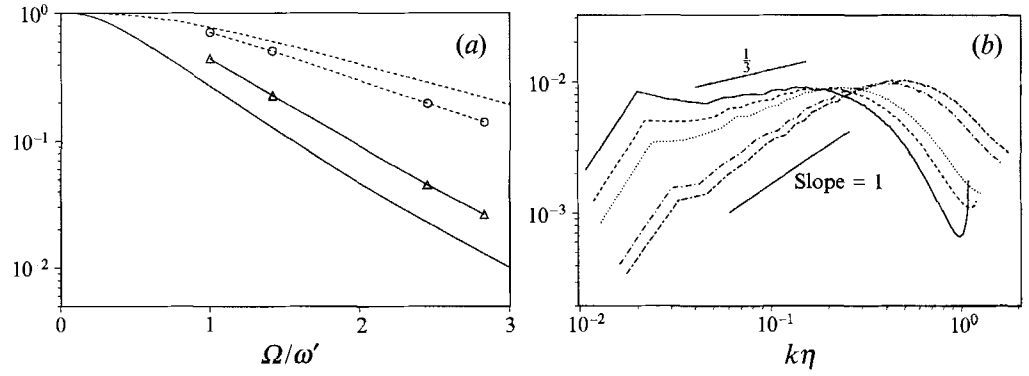

FIGURE 9. Effect of the truncation threshold on the worm fields truncated to $|\omega| > \Omega$, as described in text. (*a*) Simple solid line, volume fraction above vorticity threshold in original field; dashed, enstrophy above threshold; dashed with circles, enstrophy of truncated field, as fraction of original. Solid with triangles, kinetic energy of truncated field. (*b*) Enstrophy spectra; threshold, in order of decreasing enstrophy at low wavenumbers: $\Omega/\omega' = 0$, 1, 1.41, 2.45, 2.83. $Re_\lambda = 168$. Straight solid lines indicate power laws.

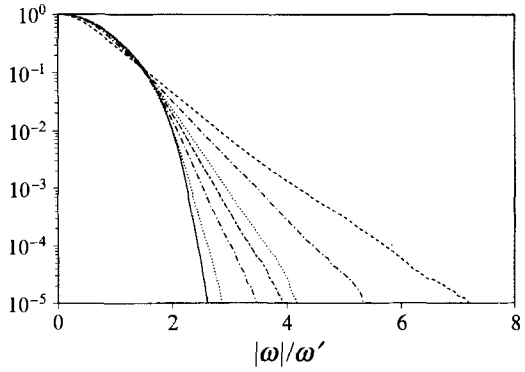

FIGURE 10. Time evolution of the histograms for the volume fraction occupied by vorticity whose magnitude is above a given threshold, during decay of a flow field initially truncated to $|\omega| < 1.5\omega'$. $Re_\lambda = 96$. Decay time, left to right: $u't/L = 0$, 0.019, 0.037, 0.056, 0.073, 0.158. All normalizations refer to the initial field before truncation, whose histogram is given by the right-most line in the figure.

vortex lines would not be closed, and no velocity could be constructed. Consider the naively truncated field

$$\omega_0 = \omega \quad \text{if} \quad |\omega| > \Omega, \qquad \omega_0 = 0 \quad \text{otherwise.} \tag{3}$$

This field is generally not solenoidal, $\nabla \cdot \omega_0 \neq 0$. We define the worms as the field $\omega_> = \omega_0 + \Delta$, such that $\nabla \cdot \omega_> = 0$, and such that the added enstrophy $\int |\Delta|^2 \, dx$ is as small as possible. Note that vorticity of this field is not strictly zero outside the worms, but that the construction guarantees that the undesired residual is a minimum. It follows from straightforward variational analysis that $\Delta = -\nabla\lambda$, where the scalar λ satisfies $\nabla^2\lambda = \nabla \cdot \omega_0$.

Note that the new field is simply the solenoidal projection of ω_0, and that a velocity can be computed from it.

The effect of this truncation is shown in figure 9(*a*), which displays both the enstrophy and kinetic energy of the truncated worm fields, as a function of the threshold, as well as the volume and enstrophy associated with regions of the original field having vorticity above that threshold. It is seen that projection decreases only

slightly the enstrophy contained in the worms. A visual check of the corresponding enstrophy isosurfaces confirms that the intense regions in the truncated field correspond to those in the original one, but that the vorticity in the background has been mostly eliminated. The energy of the truncated flow is always small, roughly proportional to the volume occupied by the worms themselves. There seems to be no appreciable local enhancement of the kinetic energy due to the presence of the worms. This is confirmed by inspection of the velocity fields in figure 7 and 8, and by the absence of Reynolds-number effects in the fluctuation velocity distributions.

Similar experiments on the truncated background fields, resulting from the removal of the vorticity above a given threshold, reveal a complementary effect. The effect of removing the worms is small, both on the enstrophy and on the energy, and it only becomes appreciable when the truncation threshold is comparable to ω'.

In addition, no particular characteristic of the energy spectrum seems to be especially associated with the worms. Figure 9(*b*) displays enstrophy spectra, $2k^2E(k)$, for the high-vorticity component at different truncation thresholds, each of them normalized by its own Kolmogorov scaling. The spectrum of the original field is consistent with an inertial range, $E(k) \sim k^{-\frac{5}{3}}$, while that of the high-intensity worms is close to $E(k) \sim k^{-1}$, but the variation of the spectrum is gradual, proportional to the removal of the total kinetic energy. The latter spectrum was shown by Townsend (1951) to be that of a random array of vortex tubes of uniform radii and is therefore consistent with the observed structure of the worms.

Since the integral of the dissipation is proportional to that of the enstrophy, the effect of removing the worms, which contain only a small percentage of the latter, is not expected to have a large effect on the decay of the kinetic energy of a turbulent field. This was tested directly by comparing the evolution of the decay from identical initial conditions with and without the worms removed. An equilibrium field was generated ($Re_\lambda = 96$) and the forcing was removed to allow decay. The same initial conditions were then truncated to $|\omega| < 2.5\omega'$, and again allowed to decay. The evolution of the energy in both cases was almost identical, when the decay rate was normalized with the initial enstrophy of each field. The enstrophy of the truncated field initially decayed faster but after a short transient, during which it decayed by about 7%, it behaved similarly to that of the non-truncated field. The difference in the total enstrophy of the initial fields at this truncation level was 20%.

A more severe truncation was applied to determine whether the presence of the worms could be somehow associated with the forcing scheme . The same flow field as in the previous experiment was truncated to $|\omega| < 1.5\omega'$, and left to decay. Figure 10 shows the time evolution of the volume-fraction histograms. It is clear that, after a short time, the worms reappear, even in the absence of forcing. This was checked directly by visualization.

It follows from these experiments that the worms are a natural product of the evolution of turbulent flows, both forced and decaying. They do not seem to play any special role, besides that which corresponds to the energy and enstrophy that they contain. At the Reynolds numbers of our experiments, both are small fractions of the total.

An interesting observation is that the skewness coefficient of the fields formed from the high-intensity regions was always negative, and roughly of the same order as that of the full turbulent field ($F_3 = -0.5$ to -1.0). The high-intensity regions do strain each other, and they are capable of generating new enstrophy, although the relatively low kinetic energy that they contain implies that the Reynolds number of the truncated flow is low.

5. The dynamics of worm formation

Although the worms do not seem to play a special role in the overall dynamics of turbulent flows, the process by which they are formed is interesting in itself. Moreover, since they appear to be part of the general $O(\omega')$ background vorticity, we may look at their generation as a particular case of the enstrophy transfer process, which is one of the central issues of the turbulence problem. Finally, since they do not scale correctly in Kolmogorov variables (i.e. the histograms do not scale with ω'), their generation mechanisms might point to some deficiency in the standard cascade theory, especially as $Re_\lambda \to \infty$.

Qualitatively, it is clear that strong vortex regions have to be formed by the straining of weaker vorticity. No other mechanism is available, away from no-slip walls, for the production of enstrophy. Strain itself is induced by the vorticity, and the process may become nonlinear. It has been realized for some time that nonlinear self-interaction of vorticity can, in principle, lead to a singularity of the inviscid equations in finite time, and that it may therefore be used to explain the generation of vorticity of almost any magnitude.

An analysis of the order of magnitude of the different processes might be relevant at this point. If we apply a strain rate α to a viscous fluid, the smallest flow features that we may expect to generate are of the order of Burgers' radius, $\delta = (\nu/\alpha)^{\frac{1}{2}}$. There are two 'natural' straining scales in turbulence: the strain rate generated by the large eddies, $1/T = u'/L$, and the inverse of the Kolmogorov timescale, which is equal to the r.m.s. vorticity $\omega' = (\epsilon/\nu)^{\frac{1}{2}}$. The Burgers' radius for the former is the Taylor microscale λ, while that for the latter is the Kolmogorov lengthscale η. Moreover, if we think of a cylindrical equilibrium Burgers' vortex, generated by a strain rate α, its peak vorticity would be $\omega_{max} \sim Re_\gamma \alpha$, where $Re_\gamma = \gamma/\nu$ is a vortex Reynolds number based on its total circulation. If we assume, for example on stability grounds, that Re_γ cannot be larger than a given limit, independent of the applied strain, the peak vorticity should never be more than a fixed multiple of the strain.

We have evidence in the histograms in figure 4 that the flow contains peak vorticities that increase with Reynolds number faster than ω'. From the previous discussion, this implies either that stretching rates higher than ω' occur, or that Re_γ increases with Re_λ. The first possibility implies that we should find structures with a transverse scale smaller than η, and that this discrepancy should increase with increasing Re_λ. This contradicts the relatively good collapse of the energy spectra in the dissipation range, expressed in Kolmogorov variables, although some weak effect cannot be ruled out from the experiments. The second possibility raises the question of how such high-Reynolds-number vortices remain stable long enough to form.

To answer this question we undertook a statistical investigation of the dimensions and circulation of the intense-vorticity structures. Most previous investigations find their radii to be a few Kolmogorov scales and their length to be of the order of the integral scale. A survey, including some new measurements of radii and intensity, is contained in Jiménez (1991). It was concluded that, for the available flow fields, the average radius was approximately 3η–5η, and $Re_\gamma \approx 150$–400. It was noted, however, that most of the data were at $Re_\lambda \approx 100$, and that no reliable Reynolds-number scaling trend could be deduced. We believe that the present investigation is the first in which enough data, with uniform resolution and overall quality, have been collected over a wide enough range of Reynolds numbers to allow a Reynolds-number scaling study.

An automatic tracking algorithm, described in detail in the Appendix, was implemented and applied uniformly to all the data fields. Briefly, a point on the worm

axis is identified as the point with maximum vorticity that has still not been assigned to any worm, and the axis is followed until either its peak vorticity falls below ω', or until the worm closes into itself or intersects another worm that has been previously followed. At each point along the axis, the vorticity in the normal plane is averaged azimuthally, and the resulting radial distribution is fitted to a Gaussian. The local radius of the worm is defined as the 1/e radius of the Gaussian, and the circulation as that of the fitted distribution. Because of the azimuthal average, it can be shown that the 'radius' computed for a ribbon or for a sheet is much close to its thickness than to its width. It was, unfortunately, impractical to continue this process until no more worms could be found, and the samples used here represent what could be achieved in a fixed amount of computer time. A rough estimate of the total volume of the worms in the sample, compared to the volume occupied by vorticity above ω', suggests that the sample contains most of the worms in the lowest-Reynolds-number case, but only about 1% of them in the highest one. Average values of worm length, radius and circulation are given in table 3. A comparison with the range of scales in table 1 is enough to show that the scalings chosen here are fairly robust, at least in this range of Re_λ, and that significantly different choices would lead to much poorer fits. In particular, the worm radii scale with η, their lengths with the integral scale L, and their circulation increases as $Re_\lambda^{\frac{1}{2}}$.

These results have to be interpreted with some care in view of the different fractions of the flow field sampled at each Reynolds number. Since each worm is initialized from the point with the most intense vorticity still unmarked, the resulting catalogue of worms is naturally ordered from the strongest to the weakest, and it is conceivable that the growth of the circulation with Re_λ may just reflect the averaging over a smaller sample at the high end of the distribution. On the other hand, circulation and vorticity along a single worm vary widely (see figure 13), and it is also possible that each worm is representative of the overall distribution of radius and vorticity, in which case the results in table 3 would be unbiased. To clarify this point, statistics were compiled for each individual worm in the sample corresponding to each Reynolds number, and the resulting mean values were analysed for intersample variability and for any trend as a function of the order in which they had been detected by the tracking algorithm. If there was a tendency for stronger worms to be detected earlier, it would be reflected as a trend in the average circulation to decrease with the order of appearance of the worm in the sample. The absence of such a trend would prove that each individual worm is representative of the whole sample, and that the statistics compiled over small samples are not biased with respect to those compiled over large ones. No significant trends were found either in the variances or in the mean values. At $Re_\lambda = 63$, where the volume fraction of the high-vorticity regions is comparable to that contained in the worms in our sample, the standard deviation among the average circulations for the 32 different worms was about 33%, and a least-squares linear fit to the averages as a function of the order of appearance gave a difference of 6% between the first and the last worm. Similar results were obtained for the other Reynolds numbers, with some sets actually increasing in circulation with order of appearance. We can therefore conclude that the statistics on which table 3 is based are not biased as a result of the sampling.

The scalings of radius and circulation are consistent with those observed in Jiménez (1991) for the intense longitudinal vortices in the wall region of a turbulent channel. It was shown there, on the basis of rather limited data, that the radii of the vortices scale well in wall units, within a range of Reynolds number $Re_\tau = 100$–200. The circulations, however, do not remain constant, and increase by a factor of almost two in the same

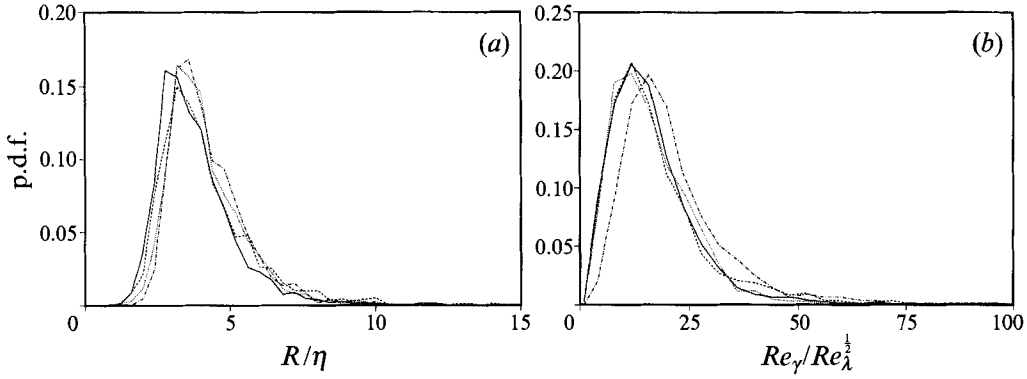

FIGURE 11. Probability density of (*a*) worm radius and (*b*) circulation at four different Reynolds numbers. Symbols as in table 1. Normalization has been chosen to optimize collapse.

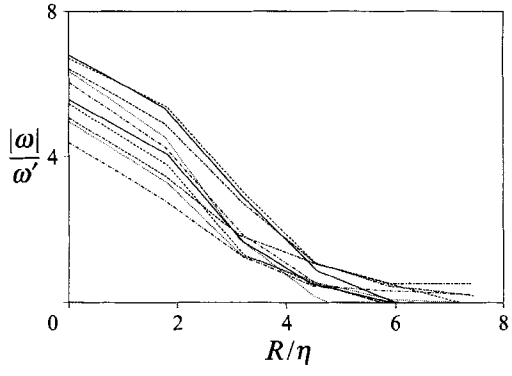

FIGURE 12. Radial vorticity distribution for different cross-sections along a typical worm. $Re_\lambda = 62.8$.

Re_λ	l/L	R/η	$Re_\gamma/Re_\lambda^{\frac{1}{2}}$	N_w
35.8	3.16	4.22	21.1	26
62.8	2.60	4.16	17.0	32
94.5	3.15	4.16	18.1	14
168.1	2.88	3.85	16.5	23

TABLE 3. Average worm characteristics, as identified by the tracking algorithm defined in the text. N_w is the number of worms in each sample, l their average length, and R their radius.

range. Since wall units are the near-wall equivalent of Kolmogorov scaling, those trends are equivalent to the ones observed here. In the same spirit, the recently established tendency of near-wall turbulent fluctuations to increase with Re_τ, beyond their dependence in wall units (Wei & Willmarth 1989), can be considered as related to the failure of Kolmogorov scaling observed in figure 4.

The actual probability density distributions of radius and circulation are given in figure 11, and a sample of azimuthally averaged vorticity profiles across a typical worm is given in figure 12, showing that the Gaussian model is at least reasonable. This model is consistent with that of an axially stretched equilibrium Burgers' vortex. The distributions of radius and circulation along the length of a few typical worms are given in figure 13 for the four different Reynolds numbers. The length is normalized with η,

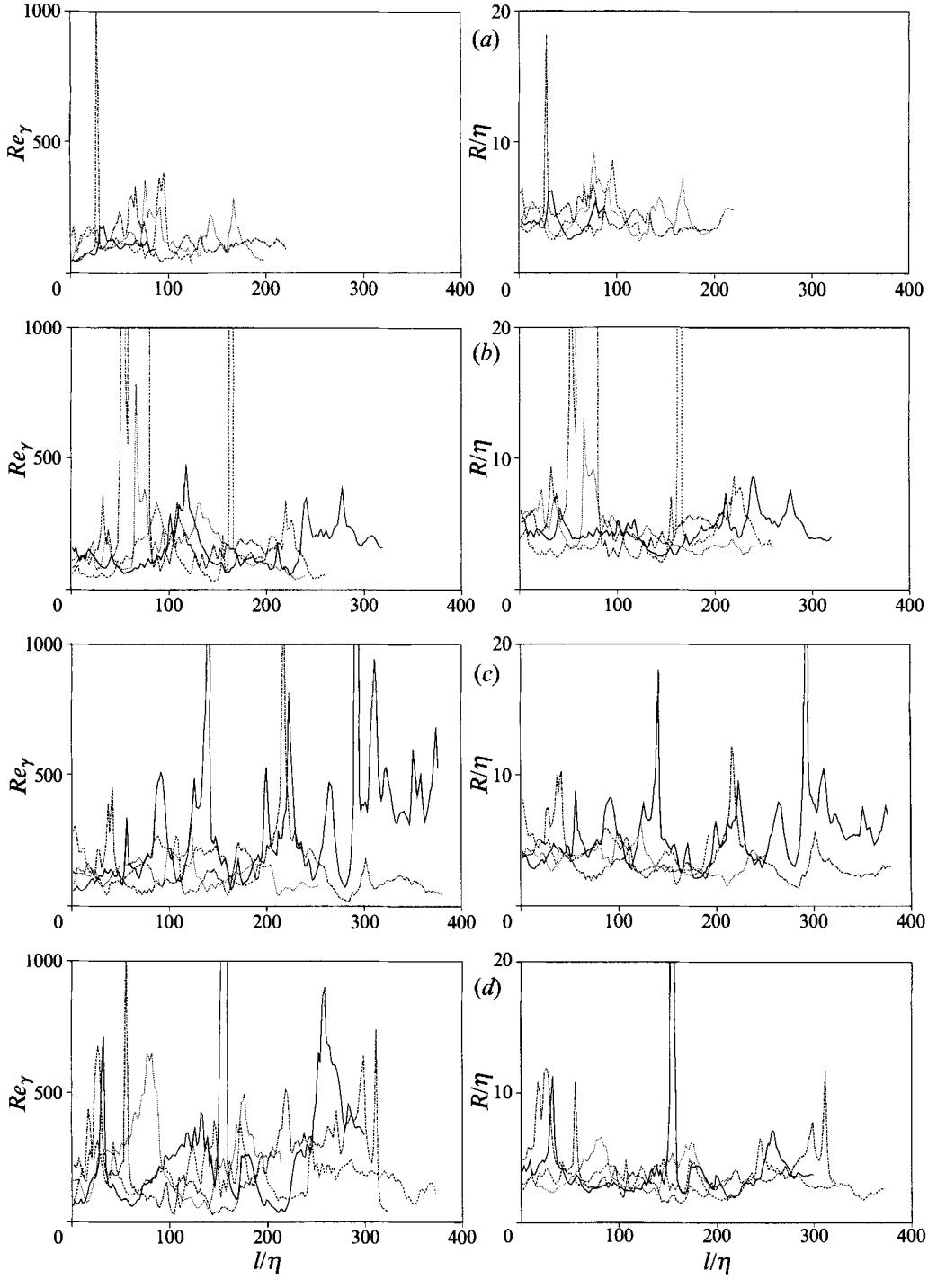

FIGURE 13. Distribution of normalized radius and circulation along worm axes, as a function of arclength l. Each figure contains four worms chosen at random. (*a*) $Re_\lambda = 35.8$, (*b*) 62.8, (*c*) 94.5, (*d*) 168.1.

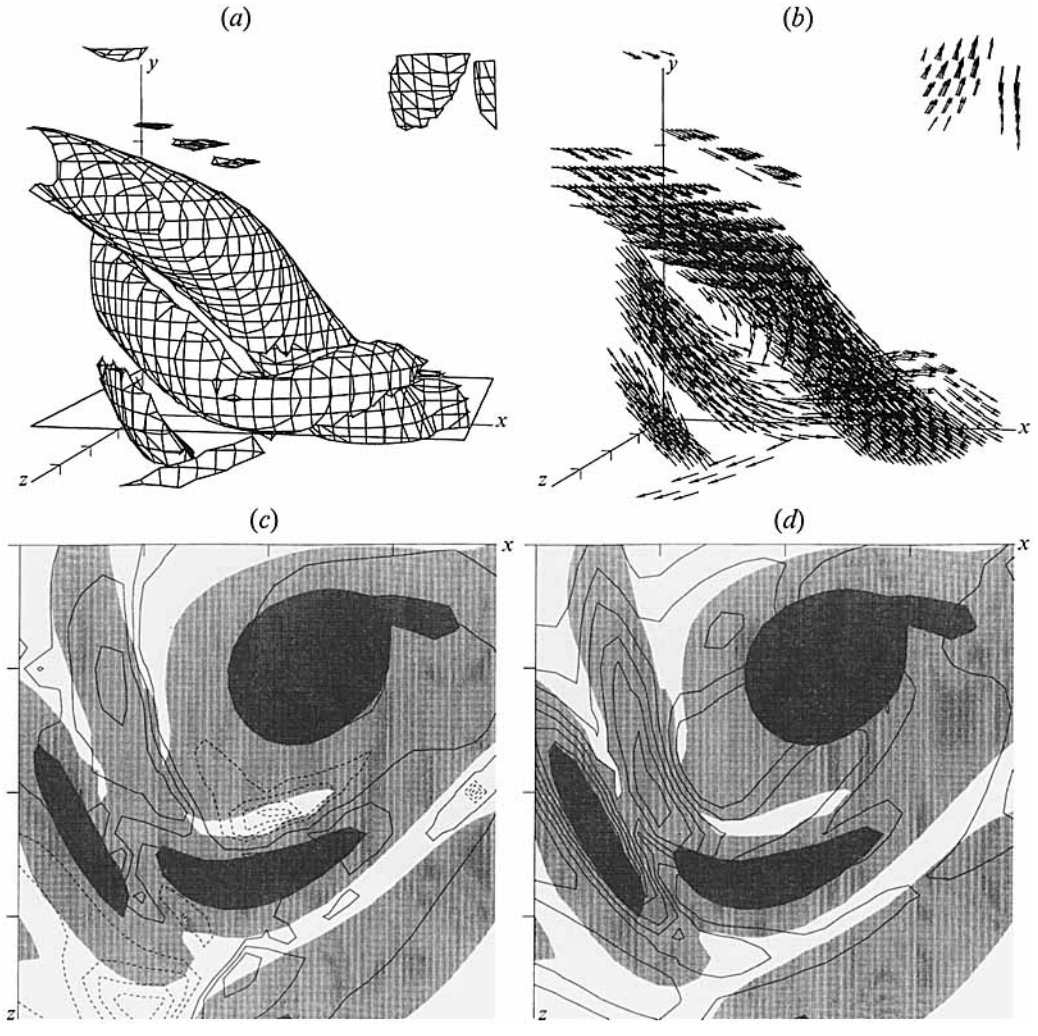

FIGURE 14. Portrait of a worm interaction, identified by a local maximum of the stretching term σ. $Re_\lambda = 94.5$. Length of axes, approximately 40η. (*a*) Intense-vorticity isosurfaces, $|\omega| = 2.8\omega'$. (*b*) Vorticity vectors within the surfaces in (*a*). Vector lengths are proportional to vorticity. (*c*) Stretching and vorticity magnitude in the horizontal plane outlined in (*a*). Isolines are σ, at $0.2\omega'$ increments; negative contours, dashed; zero contour not shown. Light grey, $\omega' < |\omega| < 2.8\omega'$; dark grey, $|\omega| > 2.8\omega'$. (*d*) Same as (*c*), but isolines are strain-rate magnitude, $|s| > \omega'$ at $0.2\omega'$intervals.

which is proportional to the mean radius of the structures, and which is the scale at which internal instabilities of the worms could first be expected to appear. It is difficult to extract general trends from this figure, and the number of actual coherent worms in each field is too small to allow for accurate statistics, but it is surprising that no obvious increase in complication is detected as Re_λ increases, even if we known from the previous analysis that higher Re_λ implies an increase in the Reynolds number of the vortices themselves. It is not clear why the worms are not becoming internally turbulent as their Reynolds number increases, and the interesting question is whether that will remain true at high enough Re_λ. This question cannot be answered directly here, but some analysis is possible on the type of complexity present in the worms in our sample. It is clear from figure 13 that the traces of circulation are noisy and, although part of

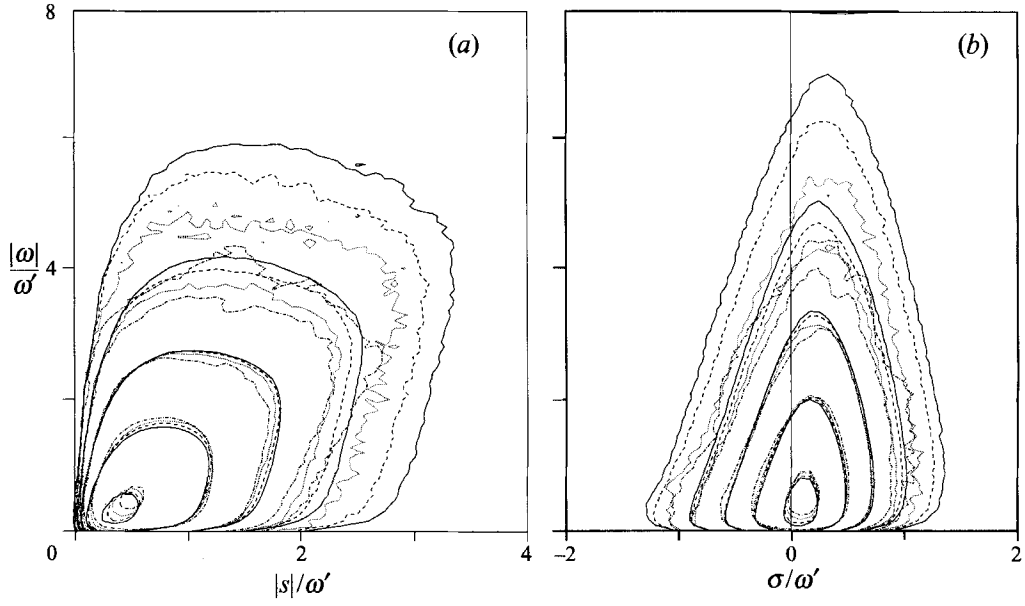

FIGURE 15. Joint probability densities of (*a*) strain-rate magnitude and (*b*) stretching, versus vorticity magnitude. All values are normalized by ω'. Density contours are logarithmic and spaced by a factor of 10. Lines as in table 1.

the noise is probably due to detection problems, some is real and survives the application of different detection algorithms. Since the circulation of a coherent vortex, defined as a fixed set of vortex lines, is constant along its length, the peaks in the circulation traces should be interpreted as interactions with other vortices.

Interactions between adjacent worms are indeed common in the flow fields, and can often be found by looking for 'active' spots in which either the vorticity or the stretching are especially large (see figure 14). Interactions between strong vortices and weaker vorticity are still more common, and they do not usually result in the destruction of the stronger partner. When the detection algorithm is applied near an interaction, the assumption of Gaussian vorticity distribution fails, which is probably the cause of the large peaks which appear in the plots. A more troubling question is whether a given structure can be identified as the same object after being tracked through an interaction. Inspection of figure 14 suggests that the central core of each vortex conserves its identity even after two vortices interact closely, but that their outer layers merge and probably exchange vortex lines (figure 14*c*, *d*). The statistics of vortex lengths in table 3 must be interpreted in this context. Worms can be traced for lengths comparable to the integral scale, but they are formed by shorter segments separated by strong interactions. It is argued below, on theoretical grounds, that this structure may correspond to their formation by accretion of smaller units.

The question of the origin of the stretching that generates the worms has still not been addressed. Figures 15 and 16 show two-dimensional joint probability density functions for vorticity magnitude and strain rate. Figure 15(*a*) compares total strain rate $|s| = (S_{ij}S_{ij})^{\frac{1}{2}}$ with vorticity magnitude. It is clear from the figure that there is a correlation between these quantities, although a rather weak one. Strong vorticity coexists with strong strain, either because strong vortices generate high strains, or because they are generated by them. That alternative is addressed in figure 15(*b*), which compares vorticity magnitude with the stretching term σ. This histogram shows that

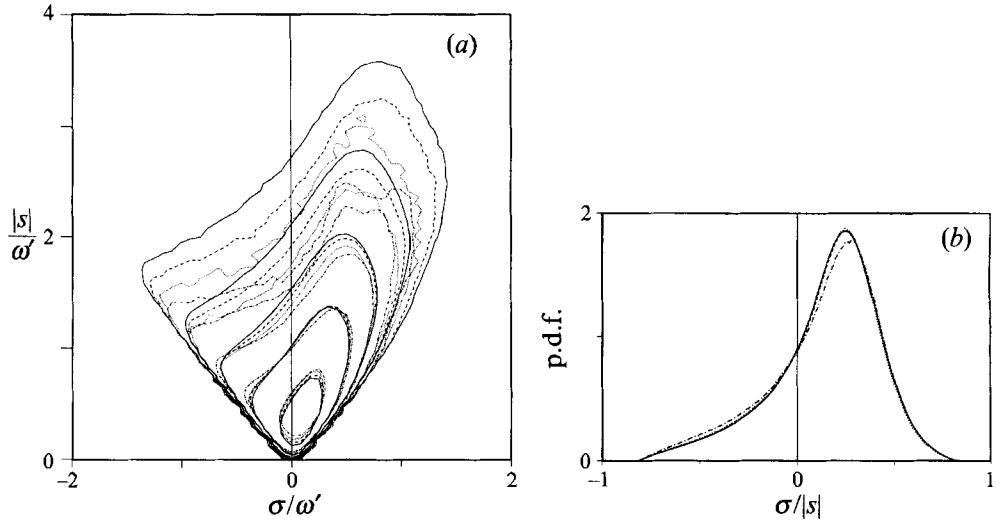

FIGURE 16. (*a*) Joint probability density of stretching versus strain-rate magnitude. (*b*) Univariate probability density of $\sigma/|s|$. Lines as in table 1.

the highest stretching rates are not associated with regions of high enstrophy, but rather with the background vorticity $O(\omega')$. In fact, the stretching associated with the highest-enstrophy regions is fairly low, with little evidence of self-stretching by the strongest structures. This apparent lack of correspondence between the behaviour of the total strain and that of the stretching component is also clear in figure 16, which compares these quantities. Although there is clearly a correspondence between high strain rate and large stretching, in the sense that strong stretching or compression is associated more often with strong strains than with weak ones, the correspondence is only moderate, and the distribution of the ratio $\sigma/|s|$ is broad, peaking at low values rather than near the extremes. This ratio can be shown to be kinematically limited to the interval $\pm(\frac{2}{3})^{\frac{1}{2}}$, which accounts for the sharp lateral cutoffs in the histograms in figure 16 but, within those limits, σ and $|s|$ are only weakly correlated. Strong strain does not necessarily mean strong vorticity compression or stretching, and the orientation of the principal axes of the rate-of-strain tensor seems to be relatively independent of the local vorticity direction. This is also seen in figure 14(*c*, *d*), in which the total strain and the stretching terms are plotted independently. The total strain rate (figure 14*d*) is relatively well correlated with the presence of strong vorticity, but the stretching is much more randomly distributed, and both strong compressions and extensions are present, close to each other. Plots of σ over larger sections of the flow field reveal a spotty distribution, with a tendency to concentrate on the periphery of background (or intense) vorticity, but not in its interior. Apparently, once vorticity is stretched to a high enough amplitude, it decouples from the original strain field and looses its orientation relative to it.

The different behaviour of $|s|$ and σ for high-vorticity regions can be quantified by examining the conditional average of each quantity over points with a given $|\omega|$, which can be derived from the distributions in figure 15 as

$$\langle \zeta; |\omega| \rangle = \int \zeta p(\zeta, |\omega|)\, \mathrm{d}\zeta \Big/ \int p(\zeta, |\omega|)\, \mathrm{d}\zeta,$$

where $p(\zeta, |\omega|)$ is the joint probability density function. While the mean rate of strain

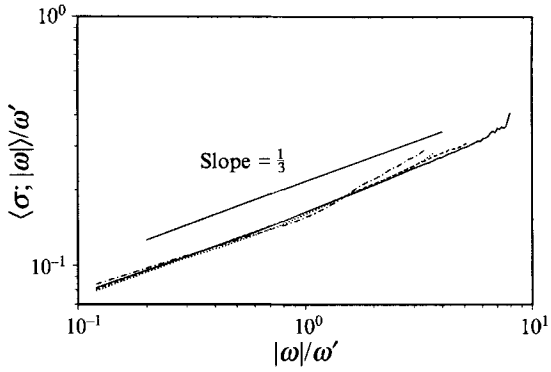

FIGURE 17. Conditional average of the stretching rate, σ, for points with a given value of the vorticity magnitude. Lines as in table 1, but short solid line represents the scaling $\sigma \sim |\omega|^{\frac{1}{3}}$.

$\langle|s|;|\omega|\rangle$ increases rapidly with $|\omega|$ (see figure 15*a*), the mean stretching $\langle\sigma;|\omega|\rangle$ increases much more slowly and, in fact, appears to scale as $|\omega|^{\frac{1}{3}}$ (figures 15*b* and 17). Note that this latter quantity appears directly on the right-hand side of the evolution equation for the total enstrophy histogram (Z.-S. She, private communication).

All of this is consistent with the result, obtained by previous investigators, that there is little preferential alignment of the vorticity with the rate-of-strain tensor at low vorticity magnitudes, and that the alignment is with the intermediate (weakest) eigenvector in the intense regions (Ashurst *et al.* 1987).

It is interesting to note that there seems to be a fairly good collapse of the distribution of $\sigma/|s|$ for different Re_λ. The distribution of σ is tilted, in both figures 16 and 15(*b*), towards positive values of σ. This asymmetry corresponds to the negative skewness of the longitudinal velocity derivatives, and makes possible the net amplification of vorticity.

One of the most striking features of these probability distributions is the similarity of their shape at different levels. The probability distributions, scaled on ω', collapse closely near the origin, corresponding to the good collapse of the one-dimensional histograms in that range. Even away from that point, where the higher-Reynolds-number cases display much stronger tails, the shapes of the distributions are very similar for the high and for the low Reynolds flows. The outer, low-probability, isolines of the low-Reynolds-number distributions coincide almost exactly with the inner, high-probability ones, at high Re_λ. This suggests again that, whatever mechanism is responsible for the generation of high-enstrophy or of high-strains regions, it is independent of Reynolds number, and that the only difference is that it becomes more common as the Reynolds number increases. The similarity of inner and outer contours also suggests that the dynamics of the intense regions is not fundamentally different from that of the $O(\omega')$ background.

6. Discussion and conclusions

We have presented measurements of the structure of the intense vorticity regions in numerical turbulent flow fields at four different Reynolds numbers, ranging from $Re_\lambda = 35$ to 170. Numerical resolution in terms of η, and running time in large-eddy turnover units, were kept as constant as possible. The fields themselves are in statistical equilibrium with a suitable forcing, and the two higher Reynolds numbers are already

in the 'asymptotic' range in which dissipation becomes independent of Re_λ. In this sense, we are dealing with true turbulent flows. These last two fields also exhibit an inertial $k^{-\frac{5}{3}}$ spectral range that, in the highest-Reynolds-number case, spans almost a decade. The collapse of all the spectra in the dissipation range, when expressed in Kolmogorov units, is excellent, although there is a suggestion of a weak trend to slightly fuller spectra at higher Reynolds numbers (figure 1). The energy spectra in this range are exponential, with an algebraic prefactor.

We give univariate histograms for several quantities related to the velocity gradients, particularly for those related to the terms of the vorticity production equation. These distributions are not Gaussian and they do not collapse in Kolmogorov units (ω'). There is a strong trend to longer tails indicating intense events at higher Reynolds numbers, which shows no signs of convergence to an asymptotic distribution within our experimental range. Comparison with experimental data at much higher Re_λ suggests that this trend continues beyond our range.

We have confirmed, in accordance with previous investigators, that the physical structure of these intense events is that of long coherent vortices, of more or less elliptical cross-section ('worms'). Although we lack adequate statistical confirmation, the eccentricity of the cross-section appears to decrease as the Reynolds number increases. We have offered an explanation in terms of the relative strength of the strain and vorticity in those regions.

By means of an automatic tracking algorithm, we have determined scaling laws for the kinematic properties of the worms. Their radii scale with the Kolmogorov microscale, their lengths with the integral scale of the flow, and their circulations increase with the Reynolds number as $Re_\gamma = \gamma/\nu \sim Re_\lambda^{\frac{1}{2}}$. With respect to this latter scaling, the data might be consistent with a slightly higher or lower exponent, but they are not consistent with the obvious hypothesis that Re_γ should remain constant.

We have tried to clarify the dynamics of worm formation by means of joint probability densities of strain rate and vorticity. As expected, high enstrophy and high strain rate are associated with one another, although rather loosely, but surprisingly the association of strong vorticity with high values of the stretching rate, $\sigma = \omega_i S_{ij} \omega_j / |\omega|^2$, is much weaker. In fact the stretching of the high-intensity worms is low, and seems to scale well with the background vorticity ω', with at most a weak $|\omega|^{\frac{1}{3}}$ dependence in its conditional average. Since the Burgers' radius for a strain rate of order ω' is $(\nu/\omega')^{\frac{1}{2}} = \eta$, this is consistent with the scaling of the radius quoted above, and strongly suggests that self-stretching is not an important factor in the evolution of the intense vorticity.

An interesting observation is that the *shapes* of the probability isolines in the tails of the joint distributions are essentially similar to those in their central parts, and that they are quite independent of the Reynolds number. This, together with the previous observation on the lack of self-stretching, suggests that the worms are merely particularly intense realizations of the background vorticity field, $|\omega| > \omega'$. This background component is responsible for most of the turbulent dissipation (80%), but fills a smaller percentage of the flow volume (25%). We have presented some indications that the background vorticity is concentrated in large-scale turbulent vortex sheets separating the energy-containing eddies at the integral scales. The worms are imbedded within this background (figures 6 and 7).

We have also shown, by removing the worms artificially from an equilibrium turbulent field and studying its further development, that worms are not especially important in the overall dynamics of turbulence, and that they are only responsible for the fraction of the kinetic energy proportional to the volume that they occupy, and for

the fraction of the dissipation proportional to their integrated enstrophy. Both fractions are small at the Reynolds numbers of our simulations, but could become larger in the limit $Re_\lambda \gg 1$. We have also shown that worms are not artifacts of forced turbulence. If they are removed from a decaying field, they reappear within a small fraction of a turnover time.

The lack of convergence of the probability distributions appears to support the multifractal models of turbulence, in which cascades of increasing intensities are concentrated on increasingly small regions of space. The way in which this local concentration occurs is somewhat surprising, but it is consistent with previous indications from the near-wall region of turbulent channels. Instead of vortices of fixed circulation being stretched more at higher Reynolds numbers, our data imply increasingly strong vortices being stretched by a fixed amount.

The question of how these vortices are formed will not be addressed here, and will be the subject of future publications. The purpose of this paper is to present a data base that can be used to constrain any such future model. It may still be of some interest to discuss briefly the nature of some of these constraints. There are three basic questions: how are the large vorticities generated, why does Re_γ increase with Re_λ, and how can small-scale structures, such as the worms, maintain a length of the order of the integral scale?

The first question presents no qualitative difficulty, although its quantitative answer lies at the heart of the turbulence theory. High vorticity is generated by stretching, and stretching is generated by the integrated effect of the rest of the vorticity in the flow. We have seen that the regions of highest vorticity have transverse dimensions of the order of η. This is already implicit in Kolmogorov theory and implies that the prevailing rate of strain is $O(\omega')$. Since we know from the histograms in figure 4 that the predominant vorticity is also $O(\omega')$, this implies that the Reynolds number of a typical dissipative eddy, Re_γ is $O(1)$ and independent of Re_λ. This is in agreement with intuitive stability arguments.

A small percentage of dissipative eddies (at our Re_λ) seem to be strained while maintaining a much larger Re_γ. Large-Reynolds-number vortex sheets are subject to inviscid instabilities, and will quickly roll into individual vortices, but columnar vortices of circular cross-section are linearly stable, although they are subject to inertial waves and will probably break up if perturbed hard enough. There is little doubt that a sufficiently high-Reynolds-number vortex will eventually become internally turbulent, but it may survive long enough to be observed in rare situations. Note also that the evidence suggests that the strong vortices are subject to rates of strain that are much weaker than their own vorticity. Under those circumstances, they would behave as essentially unstrained and they could only be appreciably perturbed by self-, or mutual, interaction.

We have seen in figure 13 that worms do not become 'noisier' with increasing Re_λ, at least within our Reynolds-number range, but it may be that only those rare vortices that do not become internally turbulent are recognized as coherent by our tracking algorithm. If the mean circulations and radii in table 3 are combined to estimate mean axial vorticities for the worms, and if these vorticities are substituted in the histograms in figure 4(*a*), it is found that the volume fraction occupied by the worms decreases slowly with Re_λ. A plausible $Re_\lambda \to \infty$ limit is one in which increasingly strong coherent structures become increasingly unlikely.

It might even be possible to shed some light on the scaling law $Re_\gamma \sim Re_\lambda^{\frac{1}{2}}$. The relation that comes to mind is

$$u'\eta/\nu \sim Re_\lambda^{\frac{1}{2}},$$

which implies that the velocity increment across an intense worm is of the same order as the characteristic velocity of the energy-containing eddies. A simple model is that of large eddies straining vorticity at the interfaces in which they meet (see figures 7 and 8). On most occasions, the vortex sheets generated in that way become unstable and break into smaller eddies that strain each other into the $O(\omega')$ vorticity background (see Moffatt 1989 and Domaradzki 1992 for related models). Occasionally, however, a small part of the vortex sheet survives the instability and is strained to thickness η while still retaining across itself the full velocity difference u'. The eventual roll-up of this sheet generates worms.

Note that this model does not predict the conditions for the formation of worms, but that it singles out the observed scaling law as an upper limit for Re_γ. Note also that it suggests that the initial stretching takes the form of sheets, since the velocity increment across a stretched sheet is maintained, while that of a cylindrical vortex increases in inverse proportion to its diameter.

Finally, the question of the long lengths of the worms is harder to answer. It is inconceivable that a rate of strain $O(\omega')$ remains coherent over a region of space of size $O(L)$. Since we know, from the lack of intermittency effects in the moments of the velocity distributions, that velocities are only $O(u')$, the largest possible coherence length for a strain ω' is $u'/\omega' \sim \lambda$. This suggests that worms are not formed in a single stage, but that they grow or coalesce during their lifetimes. Several possible mechanisms come to mind, but they are beyond the scope of this paper.

We have benefited from fruitful discussions with R. Kraichnan and S.-Z. She. We are especially indebted to J. Soria for early work in the generation of figure 15. The simulations were carried out on the NAS 128-node Intel hypercube, and at the 512-node Delta machine at Caltech. This work was initiated as part of the CTR summer programme.

Appendix. Data processing for vortex radii and circulations

In order to elucidate the geometric structure of the worms, an algorithmic definition is needed for the set of points in space which will be taken to constitute a single worm. Such definitions necessarily contain some degree of arbitrariness, and the one used here is certainly no more than one among many possibilities.

We are interested in the strong vortical regions, and we take maxima of enstrophy as starting points. We define a worm axis and core starting with:

(i) find the point of maximum enstrophy not yet included in any worm core. This is the first worm-axis point of a new worm.

From that point one could reasonably proceed along the vortex line through the point to define a worm centreline. However, an elongated region of high enstrophy, which we take intuitively as a worm, does not have vorticity perfectly aligned along its axis, nor does a given vortex line necessarily remain within it over its entire length. Therefore, to increase the chances of staying within the high-vorticity structure, the worm-core definition is taken as:

(ii) follow the local vorticity vector from the current worm-axis point until it intersects the next grid plane, then choose as worm-core points the four grid points in this plane that surround the point of intersection. The new worm-axis point is the one with the maximum enstrophy.

This is done in both directions along the vorticity vector, from the first worm-axis point until:

(iii) the worm ends when the new maximum enstrophy is below the global mean value, ω'^2, or when the worm axis intersects its own or another worm's core.

From the set of worm-axis points we compile radial distributions of axial vorticity in the next two steps:

(iv) define the normal plane around a given worm-axis point as that set of points for which the given axis point is the closest point on the worm axis;

(v) average the component of vorticity parallel to the worm axis (at the given axis point) over these radial-plane points. The averaging is done into radial bins of width Δx.

(vi) To compensate somewhat the noise introduced by the discretization of the normal plane defined in (iv), the radial distribution is averaged over triples of consecutive axial locations, using a $(\frac{1}{4}, \frac{1}{2}, \frac{1}{4})$ mask.

With the distributions of axial vorticity as a function of distance from and position along the axis, we can compute approximations to the worm radius and circulation as functions of axial position. The radial distribution is fitted to a Gaussian shape with its maximum the measured value of ω_0, the axial vorticity at the axis. The $1/e$ radius, R, of the distribution is estimated by equating the numerically computed circulation inside a small radius, $r \approx 2\Delta x$, to that corresponding to a Gaussian distribution. The circulation γ at this section is then approximated by integrating the Gaussian, assuming axisymmetry:

$$\gamma = \omega_0 \pi R^2.$$

We have found this procedure to give clearer results than computing the circulation directly from the radial distribution. The latter is hampered by the difficulty of evaluating the circulation integral over a quite noisy distribution containing vorticity from other worms and the background.

Steps (i)–(vi) are repeated to obtain a database containing a few tens of worms. Statistics of radius and circulation are collected over this database.

REFERENCES

ASHURST, W. T., KERSTEIN, A. R., KERR, R. M. & GIBSON, C. H. 1987 Alignment of vorticity and scalar gradient with strain in simulated Navier Stokes turbulence. *Phys. Fluids* **30**, 3243–3253.

BATCHELOR, G. K. 1953 *The Theory of Homogeneous Turbulence*. Cambridge University Press.

BATCHELOR, G. K. & TOWNSEND, A. A. 1949 The nature of turbulent motion at large wave numbers. *Proc. R. Soc. Lond* A **199**, 238–255.

CANUTO, C., HUSSAINI, M. Y., QUARTERONI, A. & ZANG, T. A. 1987 *Spectral Methods in Fluid Dynamics*, pp. 85–86, Springer.

CASTAING, B., GAGNE, Y. & HOPFINGER, E. J. 1990 Velocity probability density functions of high Reynolds number turbulence. *Physica D* **46**, 177–200.

CHAMPAGNE, F. H. 1978 The fine-scale structure of the turbulent velocity field. *J. Fluid Mech.* **86**, 67–108.

COMPTE-BELLOT, G. & CORRSIN, S. 1971 Simple Eulerian time correlations of full and narrow-band velocity signals in grid-generated isotropic turbulence. *J. Fluid Mech.* **48**, 273–337.

DOMARADZKI, J. A. 1992 Nonlocal triad interactions and the dissipation range of isotropic turbulence. *Phys. Fluids* A **4**, 2037–2045.

DOUADY, S., COUDER, Y. & BRACHET, M. E. 1991 Direct observation of the intermittency of intense vorticity filaments in turbulence. *Phys. Rev. Lett.* **67**, 983–986.

HOSOKAWA, I. & YAMAMOTO, K. 1990 Intermittency of dissipation in directly simulated fully developed turbulence. *J. Phys. Soc. Japan* **59**, 401–404.

JIMÉNEZ, J. 1991 On small scale vortices in turbulent flows. *CTR Ann. Res. Briefs*, pp. 45–56 (see also *Phys. Fluids* A **4**, 652–654).

KERR, R. M. 1985 Higher order derivative correlation and the alignment of small-scale structures in isotropic numerical turbulence. *J. Fluid Mech.* **153**, 31–58.

KOLMOGOROV, A. N. 1941 The local structure of turbulence in incompressible viscous fluids a very large Reynolds numbers. *Dokl. Nauk. SSSR.* **30**, 301–305.

LANDAU, L. D. & LIFSHITZ, E. M. 1959 *Fluid Mechanics.* Pergamon.

MOFFATT, H. K. 1989 Fixed points of turbulent dynamical systems and suppression of nonlinearity. In *Whither Turbulence? Turbulence at the Crossroads* (ed. J. L. Lumley) Lecture Notes in Physics, vol. 357, pp. 250–257. Springer.

RUETSCH, G. R. & MAXEY, M. R. 1991 Small scale features of vorticity and passive scalar fields in homogeneous isotropic turbulence. *Phys. Fluids* A **3**, 1587–1597.

SHE, Z.-S. 1991 Intermittency and non-gaussian statistics in turbulence. *Fluid Dyn. Res.* **8**, 143–159.

SHE, Z.-S., JACKSON, E. & ORSZAG, S. A. 1990 Structure and dynamics of homogeneous turbulence, models and simulations. *Proc. R. Soc. Lond.* A **434**, 101–124.

SIGGIA, E. D. 1981 Numerical study of small scale intermittency in three dimensional turbulence. *J. Fluid Mech.* **107**, 375–406.

SREENIVASAN, K. R. 1984 On the scaling of the turbulence energy dissipation rate. *Phys. Fluids* **27**, 1048–1051.

TOWNSEND, A. A. 1951 On the fine scale structure of turbulence. *Proc. R. Soc. Lond.* A **208**, 534–542.

VAN ATTA, C. W. & ANTONIA, R. A. 1980 Reynolds number dependence of skewness and flatness factors of turbulent velocity derivatives. *Phys. Fluids* **23**, 252–257.

VINCENT, A. & MENEGUZZI, M. 1991 The spatial structure and statistical properties of homogeneous turbulence. *J. Fluid Mech.* **225**, 1–25.

WEI, T. & WILLMARTH, W. W. 1989 Reynolds-number effects on the structure of a turbulent channel flow. *J. Fluid Mech.* **204**, 57–95.